Side Load Reduction of High Area-Ratio Nozzles

Charles E. Tinney,[†§] *John Valdez,*[†] *Joseph Ruf*[⋆] *and Travis Rivord*[⋆]
[†]*Applied Research Laboratories, The University of Texas at Austin*
Austin, USA, 78758
[⋆]*ER42/Fluid Dynamics Branch, NASA Marshall Space Flight Center*
Hunstville, USA, 35812
[§]Corresponding Author: charles.tinney@arlut.utexas.edu, https://www.arlut.utexas.edu/gdl

Abstract

A laboratory scale evaluation of off-axis side-loads generated by a high area-ratio thrust optimized parabolic contour nozzle during startup is discussed. Nozzle side-loads are generated by well known shock patterns and transition states comprising free-shock separated flow (FSS), restricted-shock separated flow (RSS), and an end-effects regime (EER). Modifications to the test hardware are evaluated in the form of changes to nozzle scale, nozzle wall roughness, as well as the insertion of pressure relief ports near the nozzle lip. The findings demonstrate sensitivities to both FSS to RSS transition, and EER side-loads on account of nozzle wall roughness and the insertion of wall pressure relief ports. For the smooth wall nozzle, fore and aft motions of the separation shock near the nozzle lip during EER generates pressure changes (peak to valley) that are approximately 1.3 atmospheres. For the same nozzle contour with rough wall, the pulsations reduce to 0.50 atmospheres with additional reductions (down to 0.32 atmospheres) being invoked by the insertion of pressure relief ports in the vicinity of the EER shock. EER pressure loads are also delayed to higher nozzle pressures due to wall roughness effects and pressure relief ports. Where off-axis side loads are concerned, the pressure relief ports provide a 35% reduction in peak nozzle side loads during FSS to RSS transition, and a 31% reduction during EER, relative to the rough wall nozzle. It is postulated that the pressure relief ports are effective at reducing nozzle side loads as they provide a pathway for transferring flow mass from within the separation bubble to the low pressure regions of the nozzle located upstream of the wall shock during EER.

1. Introduction

Many modern-day space launch vehicles use large area ratio rocket nozzles with thrust-optimized parabolic (TOP) contours due to their excellent thrust-to-weight ratio at vacuum. However, during startup, the internal flow within the TOP nozzle progresses through a series of flow and shock wave patterns that produce both lateral and vibroacoustic loads on the vehicle and surrounding structure.[1–4] For some TOP nozzles, this comprises both free-shock separated flow (FSS), restricted-shock separated flow (RSS), and an end-effects regime (EER) where nozzle pressure ratio (NPR, the ratio of plenum pressure p_0 to atmospheric pressure p_a) is the key determinant of the flow state. Deflections in the nozzle wall exacerbate the problem by provoking an aeroelastic coupling between the fluid dynamics and structural dynamics.[5–8] These unsteady loads have been responsible for premature failure of mission critical vehicle components, all the while increasing the likelihood of additional launch debris. For this reason, rocket nozzle flow control devices have been the subject of interest since the inception of the rocket motor.

One of the earliest known studies of rocket nozzle control devices to have been released to the scientific community is the one by Foster and Cowles (1949),[9] which focused on inducing rocket motor nozzle flow separation at a desired area ratio for improved thrust. Foster and Cowles (1949)[9] evaluated ablative materials, an assortment of annular (azimuthal) arrays of holes (with/without grooves, and passively/actively-forced gas), abrupt changes to the nozzle wall contour (the impetus for the dual-bell nozzle concept[10,11]), as well as movable sections of the nozzle that could slide into position at predetermined pressure ratios. Some success was obtained at anchoring the separation shock location, though no mention of their impact on nozzle side loads was reported. Since this early work, nozzle side loads have become a problem of practical importance for sea-level launch vehicles while many of the concepts proposed by Foster and Cowles (1949)[9] have since been revisited and have demonstrated sizable reductions in peak off-axis side loads. For example, Legros et al. (2022)[12] performed subscale measurements on dual-bell nozzles combined with fluidic injection near the junction between the two bells and reported a reduction in lateral forces to less than 1% of the nozzle thrust while allowing the transition nozzle pressure ratio to be increased by nearly 24%. Annular slots that vent atmospheric gases to the low pressure zone immediately downstream of the separation shock, or that draw high pressure gases from

the combustion chamber, have been studied numerically by Ivanov and Kryukov (2019),[13] while Hadjadj et al. (2015)[14] evaluated the effect of film cooling on the separation shock and noted its potential use for nozzle side load reductions. Stark and Génin (2011,2016)[15,16] proposed a ring shaped device (different from any of the devices proposed by Foster and Cowles 1949[9]) to serve as an extension to the nozzle wall (to be installed on the test facility and launch pad) and recorded nearly 25% peak side load reductions during FSS→RSS transition of a cold flowing subscale TOP nozzle.

In the current study, we assess the utility of a new side load reduction device that leverages pressure relief ports embedded in the nozzle wall that provide a feedback loop between the low and high pressure regions upstream and downstream of the separation shock. This was prompted by an effort initiated in 2016 by Tinney et al. (2017)[7] where several laboratory-scale nozzles, fabricated from elastomeric materials with varying shore values, were evaluated to show that even small amounts of wall compliance can have a profound impact on the behavior of the shock pattern as well as the vibroacoustic loads that it generates. Thus, a device that passively reduces nozzle side loads by leveraging the sensitivity of the separated flow and shock pattern location to small disturbances at the nozzle wall seems promising. In order to relax fabrication costs, the prototype concept is constructed from additive manufacturing techniques (AMT). However, AMT materials introduce additional factors in the form of surface roughness effects, which have to be accounted for if the effectivensss of the nozzle side load reduction device is to be understood. As such, a series of laboratory-scale TOP nozzles comprising smooth/rough walls, and with/without pressure relief ports located near the nozzle lip, are evaluated for pressure ratios covering the different shock pattern transition states responsible for generating peak nozzle side-loads.

An outline of this study is as follows. A description of the facility and test hardware is first provided including details concerning the pressure relief port concept. The instruments used to quantify nozzle side loads are then described including the calibration process and sources of uncertainty. Preliminary findings from experiments that employ conventional laboratory diagnostics (static and dynamic wall pressure, nozzle side load sensing system) during startup and shutdown of the nozzles are then discussed. This is followed by an evaluation of the effect of wall roughness and the new pressure relief ports on the unsteady wall pressure near the nozzle lip during EER. A comparison of nozzle side loads generated by the different test hardware are then evaluated for nozzle startups with an emphasis on FSS→RSS and EER flow states. Plausible explanations of how these wall pressure relief ports invoke changes to off-axis side loads are then offered with concluding remarks.

2. Experimental Setup

2.1 facility

All measurements were acquired in the Gas Dynamics Laboratory (GDL) of the Applied Research Laboratories, The University of Texas at Austin (ARL:UT). The GDL houses several high pressure test stands in an acoustically treated facility enclosing approximately 31,100 ft^3 (850 m^3) of air space. The high pressure gas delivery system functions as a blow down type with pressurized gas being stored in several vessels comprising 220 ft^3 (6.2 m^3) of water volume storage at 2,100 psig (143 atm). Condensate separators remove oil and water during high stages of compression, while the total temperature of the unheated air is based on the outside temperature of that day. The average outside temperature for these tests was found to be 80 F (300 K) which equates to a ratio of specific heats of $\gamma_j = 1.4$, a specific gas constant for air of $R = 287.05$ J kg^{-1} K^{-1} and a sound speed of 347 m/s. A horizontal nozzle test stand located in the center of the GDL is used for these studies. The test stand elevates nozzle hardware 100 inches from the laboratory floor with nozzle exhaust plumes exiting the facility through the center of a large opening in the GDL wall. Outside air is allowed to enter the facility through additional openings located behind the nozzle test stand. Total temperatures T_0 and pressures P_0 in the plenum are monitored and recorded during each test run and are aligned with test data during post processing. For high area ratio nozzles, an assortment of Scanivalve DSA3218 Digital Pressure Scanners are used to record the static wall pressure p_s inside the nozzle. Each module incorporates 16 temperature compensated piezoresistive pressure sensors with an accuracy of ±0.05% FS that are digitized using 16 bit A/D converters; see Valdez and Tinney (2018)[17] for details concerning the GDL and its test apparatus.

2.2 nozzle hardware

Over the years, numerous nozzles have been tested at the GDL for projects ranging from supersonic jet noise[18] to side-loads and viboracoustic loads of high area ratio nozzles.[19–23] For this study, a thrust optimized parabolic (TOP) contour nozzle designed by Ruf et al. (2009)[24] was used as it has been shown to generate both free-shock separated (FSS) and restricted-shock separated (RSS) flow states during start up, as well as an end-effects regime (EER) at moderate pressure ratios. The two prominent sources of side-loads are caused by FSS→RSS transition as well as EER.

no.	nozzle	x_L [inch]	D^* [inch]	D_e [inch]	material	surface [μm]	kulite	P-wall	loads
1	smooth-wall (large)	9.375	1.5	8.255	AL-6061	20 - 40	—	●	—
2	smooth-wall (small)	3.125	0.5	2.752	AL-6061	0.1 - 0.4	●	●	●
3	rough-wall	3.125	0.5	2.752	SLSN	40	●	●	●
4	ported-wall	3.125	0.5	2.752	SLSN	40	●	●	●
5	tare	3.125	0.5	0.402	SLSN	40	—	—	●

Table 1: **Summary of nozzle hardware tested.**

The TOP nozzle contour is shown in Fig. 1a and comprises an area ratio of $A/A^* = 30.29$, a radius of curvature at the throat of $r_c = r^*$ as well as an initial expansion angle of $\alpha_c = 40$ deg that eventually relaxes to $\alpha_e = 7$ deg at the nozzle lip.

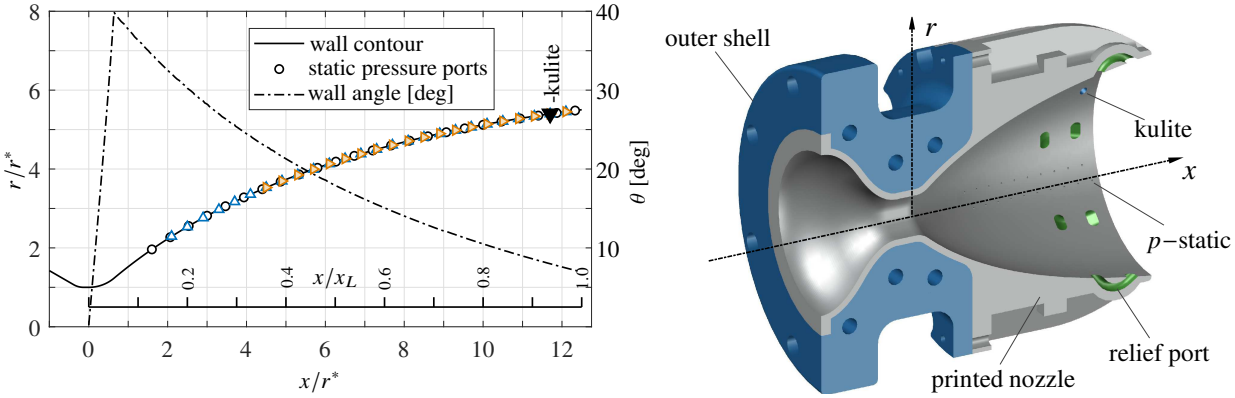

(a) (b)

Figure 1: (a) Thrust optimized parabolic nozzle contour with wall angle [deg] and location of static pressure sensing ports for the different nozzles. (b) Cross-section of additive manufactured rough-wall nozzle and its major components.

Several variants of this nozzle contour were tested for this study and ranged from changes to nozzle scale, nozzle wall surface roughness and the insertion of wall pressure relief ports. Some of the nozzle characteristics are provided in Table 1 and are described as follows.

1. Smooth wall. Two different scale nozzles, both fabricated from 6061 aluminum alloy (A96061) to have smooth walls, were evaluated to gauge the effect of nozzle scale. The first of these (no. 1 in Table 1) is the larger of the two scales and is used primarily as a standard for comparing static wall pressure measurements to for all nozzles. This large, smooth-wall TOP nozzle has a throat diameter of $D^* = 1.5$ inch and is outfitted with twenty-four static wall pressure sensing ports between $0.128 \leq x/x_L \leq 0.987$, as shown in Fig. 1a (circle symbols). A geometrically scaled replica of the larger TOP nozzle was then fabricated at 33% scale to have a throat diameter of $D^* = 0.5$ inch (no. 2 in Table 1). This 33% scale nozzle is the same one used by Rojo et al. (2016)[23] and Canchero et al. (2016)[22] and is outfitted with twenty-six static pressure ports located from $0.168 \leq x/x_L \leq 0.968$, as shown in Fig. 1a (triangle symbols). As such, most of our discussion will focus on the small smooth-wall TOP nozzle whose nozzle length x_L is valued at 3.125 inch (79.375 mm) and is measured from the throat where $r^* = 0.250$ inch (6.35 mm), to the nozzle lip where $r_e = 1.376$ inch (34.95 mm). For the remainder of this discussion, any reference to a smooth-wall nozzle will be the smaller of the two smooth-wall scale nozzles listed in table 1, unless explicitly stated otherwise.

2. Rough wall. The same 33% scale geometry used for the small smooth-wall nozzle was then fabricated using additive manufacturing methods (selective laser sintered nylon -SLSN). These are identified by nos. 3-4 in Table 1 and provided an inexpensive way of fabricating different passive side-load reduction devices. The SLSN material has an estimated average surface roughness of 40μm, as provided by the manufacturer, which is higher than the estimated surface roughness of the smooth-wall nozzle (0.1-0.4μm). Thus, the SLSN material may have a potentially more significant impact on the boundary layer and shock wave behavior at this scale. Furthermore, because of the lower yield strength of the SLSN material relative to ferrous materials, an aluminum alloy outer shell was fabricated to reinforce regions along the SLSN nozzle wall where pressure loads are high, (where the

subsonic plenum resides and in the vicinity of the nozzle throat). The outer shell also provide a rigid face for securing the SLSN nozzle to the plenum face. A cutaway of the design (using nozzle no. 4 as an example) is provided in Fig. 1b where the SLSN material is seen to extend from the beginning of the subsonic contraction, to the end of the supersonic nozzle lip. This one piece design prevents shocks from forming at junction points. However, the use of a reinforcing outer shell limited the placement of static pressure sensing system to twenty ports between $0.360 \leq x/x_L \leq 0.968$.

Two SLSN nozzles are evaluated here, the first serving as a baseline shape (rough-wall) with no modifications to the nozzle wall (no. 3 in Table 1). The second (no. 4 in Table 1) has an azimuthal array of eight pressure relief ports where x_1 and x_2 are the locations of the upstream and downstream ports measured from the nozzle throat and are valued at $x_1/x_L = 0.775$ and $x_2/x_L = 0.918$. The port cross-section measures 0.1×0.2 inch with 0.05 inch radius filleted corners which results in a cross-section area of $A_p = 0.0179$ inch^2 (11.52 mm^2). This equates to a ratio of the throat area as $A_p/A^* = 0.091$. The location of the pressure relief ports on the ported-wall nozzle were specifically chosen to bridge the wall pressure before and after the separation shock foot when the nozzle undergoes EER.

3. Tare nozzle. The last of the nozzles tested, also fabricated from SLSN, is a tare nozzle and was used to separate flow and facility related effects from off-axis side-loads generated by shock-related effects. This tare nozzle shares many of the same features as the 33% scale nozzles in terms of nozzle length, throat diameter and throat location. However the contour of the tare nozzle contracts linearly from the nozzle throat to the nozzle lip so that the flow remains subsonic until the exit. Thus, the tare nozzle quantifies side-loads generated by subsonic boundary layer effects.

2.3 strain tube

Nozzle side-loads are measured using a strain tube following the same technique described by Dumnov[25] and Ruf et al.[5,24,26] The strain tube is a flow through type that also serves as the nozzle plenum and with the nozzle hardware cantilevered on the end of the strain tube. If the axial location of the side-load is known, then forces can be converted to moments, and vice versa, as follows,

$$\begin{bmatrix} M_y \\ M_x \end{bmatrix} = \begin{bmatrix} F_x \\ F_y \end{bmatrix} \begin{bmatrix} L \\ L \end{bmatrix} \tag{1}$$

where L is the distance from the strain tube flange face to the location of the applied load. Calibrations are performed using second-order least squares regression and for the F_x and F_y components of the force vector independently. The arrangement of strain gauge pairs on the strain tube is shown in Fig. 3 with coordinate system. The mathematical framework for calibration relates the x-component force f_x to sensor voltages v_1 and v_2 by way of f_{x1} and f_{x2}, respectively, while the y-component force f_y is related to sensor voltages v_1 and v_2 by way of f_{y1} and f_{y2} as follows.

$$f_{x1} = (a_{x1}v_1^2 + b_{x1}v_1 + c_{x1}) \tag{2}$$
$$f_{x2} = (a_{x2}v_2^2 + b_{x2}v_2 + c_{x2}) \tag{3}$$
$$f_{y1} = (a_{y1}v_1^2 + b_{y1}v_1 + c_{y1}) \tag{4}$$
$$f_{y2} = (a_{y2}v_2^2 + b_{y2}v_2 + c_{y2}) \tag{5}$$

The first step to solving this algebraic system of equations is to rearrange the linear and quadratic coefficients that make up the right hand sides of Eqs. (2) through (5) into matrix form as follows,

$$[W_b] = \begin{bmatrix} b_{x1}^{-1} & b_{x2}^{-1} \\ b_{y1}^{-1} & b_{y2}^{-1} \end{bmatrix} \tag{6}$$

$$[W_a] = \begin{bmatrix} a_{x1}^{-1} & a_{x2}^{-1} \\ a_{y1}^{-1} & a_{y2}^{-1} \end{bmatrix} \tag{7}$$

where $[W_b]$ and $[W_a]$ are the first and second order polynomial coefficient matrices, respectively. Instead, we want the inverse of Eqs. (6) and (7),

$$[W_B] = [W_b]^{-1} = \begin{bmatrix} B_{x1} & B_{x2} \\ B_{y1} & B_{y2} \end{bmatrix} \tag{8}$$

$$[W_A] \quad = \quad [W_a]^{-1} = \begin{bmatrix} A_{x1} & A_{x2} \\ A_{y1} & A_{y2} \end{bmatrix} \tag{9}$$

so that $[W_b][W_B] = [I]$ and $[W_a][W_A] = [I]$. The $x-$component and y-component forces can now be estimated based on contributions from f_{x1} and f_{x2}, and from f_{y1} and f_{y2}, respectively,

$$F_x = (A_{x1}v_1^2 + B_{x1}v_1 + C_{x1}) + (A_{x2}v_2^2 + B_{x2}v_2 + C_{x2}) \tag{10}$$

$$F_y = (A_{y1}v_1^2 + B_{y1}v_1 + C_{y1}) + (A_{y2}v_2^2 + B_{y2}v_2 + C_{y2}) \tag{11}$$

or by combining Eqs. (10) and (11) in terms of quadratic, linear, and y-intercept coefficient matrices as follows

$$\begin{bmatrix} F_x \\ F_y \end{bmatrix} = \begin{bmatrix} A_{x1} & A_{x2} \\ A_{y1} & A_{y2} \end{bmatrix} \begin{bmatrix} v_1^2 \\ v_2^2 \end{bmatrix} + \begin{bmatrix} B_{x1} & B_{x2} \\ B_{y1} & B_{y2} \end{bmatrix} \begin{bmatrix} v_1 \\ v_2 \end{bmatrix} + \begin{bmatrix} C_{x1} & C_{x2} \\ C_{y1} & C_{y2} \end{bmatrix} \tag{12}$$

After dropping the y-intercept term in Eq. (12), the full matrix form is written as

$$[\mathbf{F}] = [\mathbf{W_A}]^{-1} [\mathbf{V}]^2 + [\mathbf{W_B}]^{-1} [\mathbf{V}] \tag{13}$$

For the remainder of this discussion, F_x and F_y are the applied forces, v_1 and v_2 are input voltages from strain gauges 1 and 2, respectively, while $\hat{F}_x$ and $\hat{F}_y$ are force estimates obtained from Eq. (13) and by way of coefficient matrices $[W_A]$ and $[W_B]$.

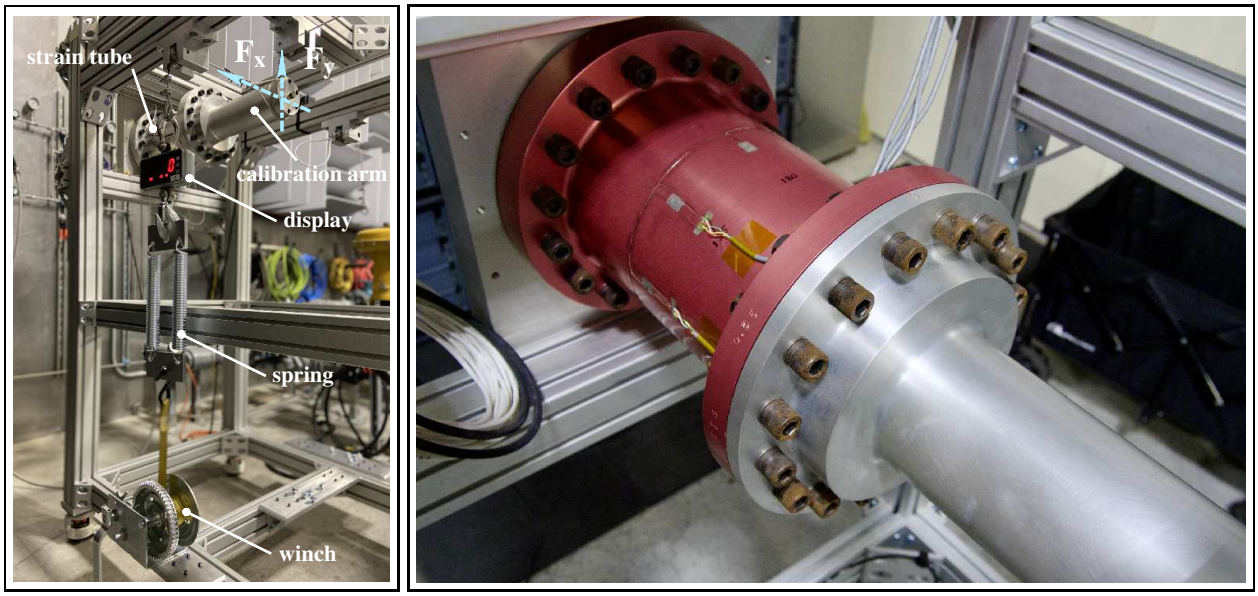

Figure 2: (a) Calibration cage with strain tube. (b) Strain tube and calibration arm during calibration.

2.4 calibration procedure

Calibrations were performed by gradually applying positive and negative forces F_x and F_y at the end of the calibration arm as shown in Fig. 2a and 3a, where $L_c = 22$ inches. The process was repeated for ±200 lbf and ±400 lbf force ranges, and with elevated plenum pressures (0 psig and 650 psig plenum pressures) which was found to affect the slope of the strain tube response to within 5% of the full-scale load range. Gas temperatures were also recorded, though there were no observable changes with respect to changing gas temperatures. Strain gauge voltages were then digitized synchronously with an S-beam load cell (Omega model LC103B-1K with 1000 lbf range and ±0.02% full-scale accuracy). A demonstration of the calibration is shown in Fig. 4a,b during both loading and unloading of F_x and F_y component forces, respectively. As expected, for the F_x component forces in Fig. 4a, the G_1 gauge reads zero since it is orthogonal to the $x-$direction and is only sensitive to F_y components loads (see Fig. 2b). Likewise G_2 and G_4 are oriented at 45 deg so they are responding nearly identically to the applied load, as expected, while G_3 demonstrates the greatest sensitivity. One can apply the same logic to Fig. 4b where the response of strain gauges to loading and unloading with F_y component forces are concerned.

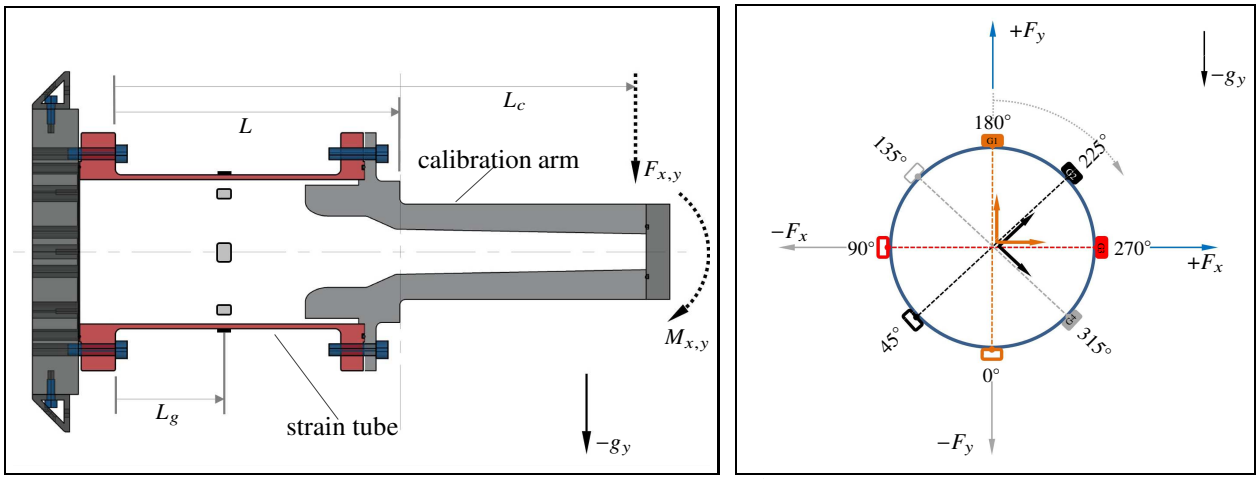

Figure 3: (a) Strain tube method with coordinate system. (b) Arrangement of strain gauges.

F_x and F_y component forces were then determined by stitching together data strings for both the positively and negatively applied forces using second-order expressions. Load measurement accuracy is determined by subtracting estimated loads (using second order methods) from measured values, as shown in Fig. 4c,d for the F_x and F_y component forces, respectively. One can see that errors are generated by hysteresis effects and can be reduced by reducing the full-scale load range.

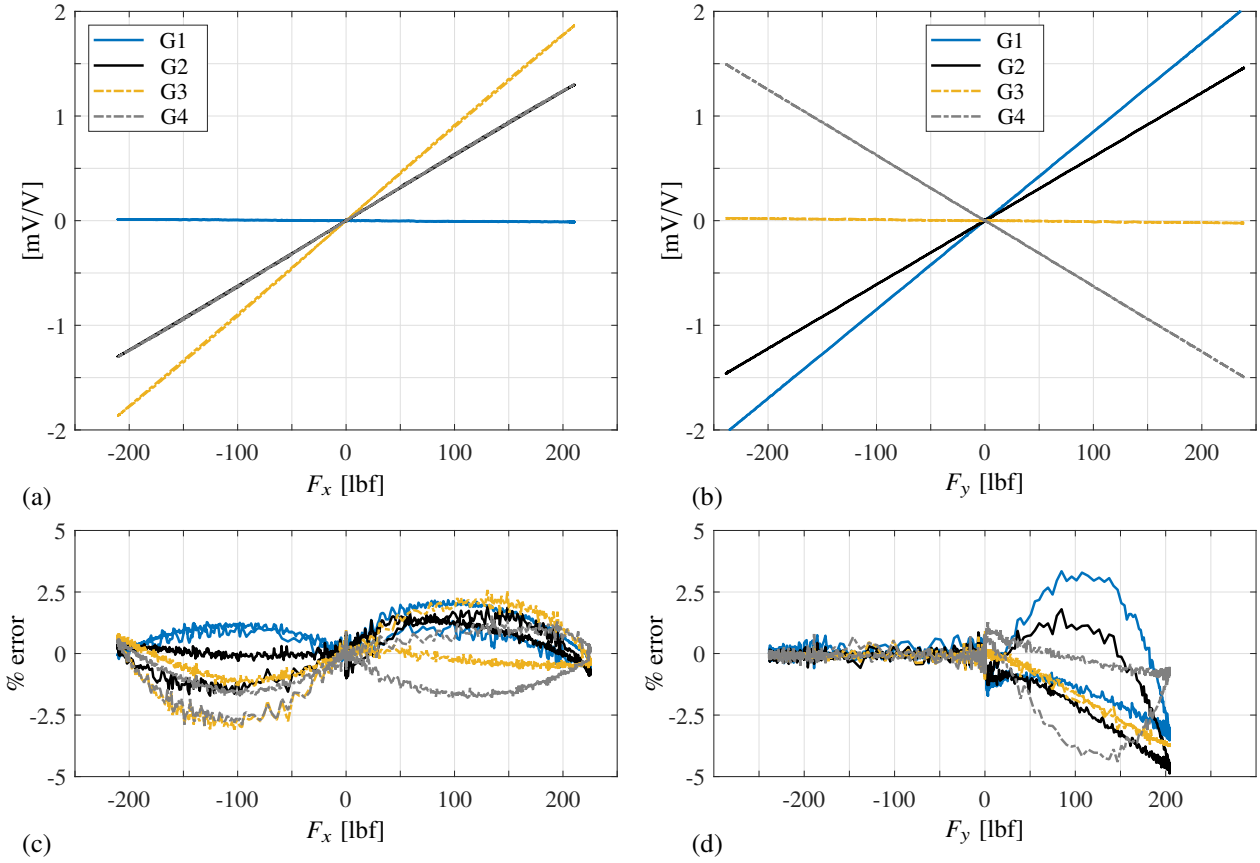

Figure 4: Calibration loads and responses. (a) F_x and (b) F_y and their corresponding errors based on full-scale output range.

3. Results

Several startups and shutdowns of each nozzle were used to develop a statistical representation of nozzle side loads during which plenum temperatures and pressures, atmospheric pressure in the facility, as well as voltages from the strain gauges on the strain tubes, were digitized synchronously at a rate of 2kS/s. Nozzle static wall pressures were captured using two Scanivalve modules at a rate of 448 Hz (triggered and synchronized using an external TTL signal) and then resampled using piecewise polynomial interpolation to match the 2kS/s sample rate of the other systems. These particular modules collectively cover three pressure ranges from 0 to 300 psig (module 1 channels 1 through 8 starting near the nozzle throat), 0 to 50 psig (module 1 channels 9 through 16), and then 0 to 15 psia (module 2 channels 17 to 32 towards the exit of the nozzle).

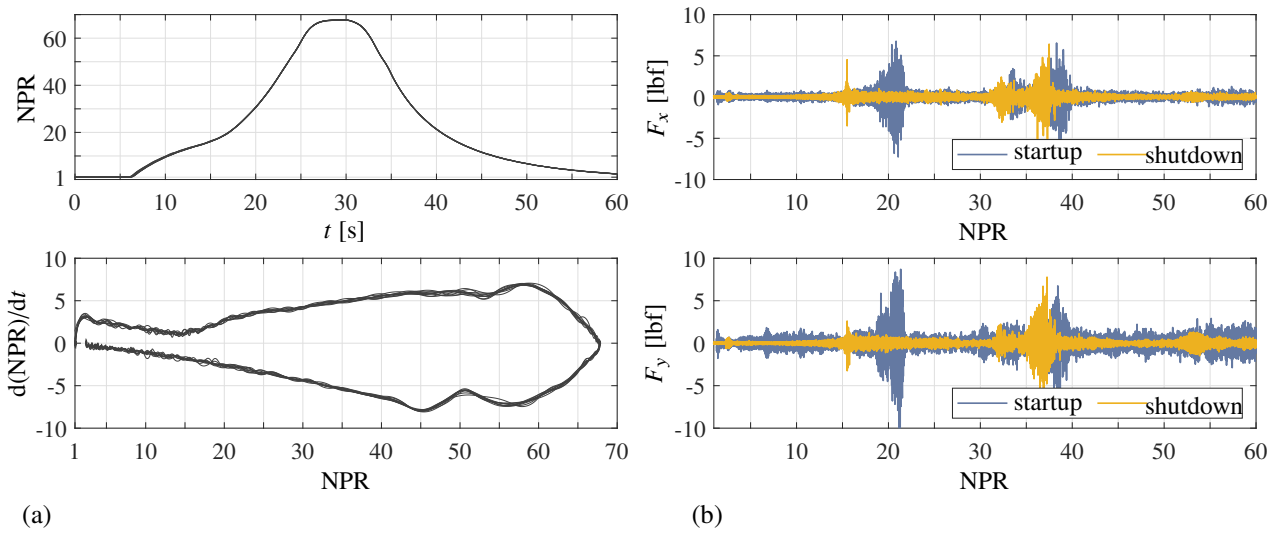

Figure 5: (a) Nozzle pressure ratio and its time derivative during testing. (b) sample nozzle side-loads during startup and shut down.

Typical NPR curves, and their time-derivatives, are shown in Fig. 5a for ten tests using the same ramping function and gas-storage starting pressure. This improves the repeatability of testing while reducing variations between NPR curves to within the thickness of the plotted line. The startup rate is shown to increase fairly linearly from 2.5 NPR/s at NPR = 20, to a peak of 7.5 NPR/s at NPR = 55, therefore resulting in an average change of approximately 0.14 NPR/s^2. A total of ten tests of the tare nozzle were performed, while twenty-five tests for each of the other three nozzles (smooth-wall, rough-wall, and ported-wall) were acquired and was found to provide a statistically accurate representation of nozzle side-loads according to the goals of this exploratory study. Moments measured by the strain tube using Eq. (1) are then converted to side-loads by multiplying the strain tube output (converted to engineering units using Eq. (13) with proper calibration coefficients) by the ratio of $L/(L^* + l_p)$ where L is the distance from the strain tube flange at $z = 0$ to the nozzle throat (valued at 24.25 inch) and l_p is the axial distance from the nozzle throat at $z = L^*$ to the location static pressure port where the separation shock resides; all off-axis side-loads are assumed to be generated by the separation shock whose location is easily identified by the first large rise in static wall pressure from its minimum value. A sample demonstration of measured nozzle side-loads is shown in Fig. 5b using the small-baseline nozzle as an example. These loads are separated into F_x and F_y component forces and for both startup and shutdown of the nozzle. Both components of the force vector are nearly equal in magnitude and demonstrate how nozzle side-loads are isotropic. The large isolated jumps correspond to off-axis side-loads being generated by the different flow and shock patterns that form during startup and shutdown.

3.1 Static wall pressure

Turning one's attention to Fig. 6, the static wall pressure (expressed as p_s/p_a) that forms during startup of this TOP nozzle (NPR$\rightarrow \infty$) is shown. This is demonstrate using the large smooth-wall nozzle as it encompasses the broadest coverage of pressure sensing ports, relative to all other nozzles used in this study. Wall pressure profiles are unique to the nozzle contour while the location of the separation shock is different for the occasion when the nozzle is shutting down (NPR$\rightarrow$ 1). For this study, only startup loads are discussed. A timeline of events describing the different flow

and shock patterns that form during nozzle startup is also shown immediately below; see Canchero et al. (2016)[22] for a more detailed discussion. At low nozzle pressure ratios, the free-shock separated flow state is observed and with FSS→RSS transition occurring around NPR 22 for this TOP nozzle. FSS→RSS transition is provoked by the strengthening of a Coanda effect which attracts the separated supersonic shear layer to the nozzle wall. The RSS flow state encompasses three annular separation bubbles corresponding to a series of compression and expansion waves that trap low and high pressure pockets of gas. FSS→RSS transition also causes the compression and expansion waves to attach to the wall far downstream from where the FSS separation shock resided immediately prior to FSS→RSS transition. As NPR increases, each annular separation bubble is pushed out of the nozzle. The higher-than-ambient pressure in each bubble induces a fore and aft motion of the separation shock location, which serves as the bubble's upstream boundary. Azimuthal asymmetries in the rapidly changing separation shock location invoke off-axis loads,

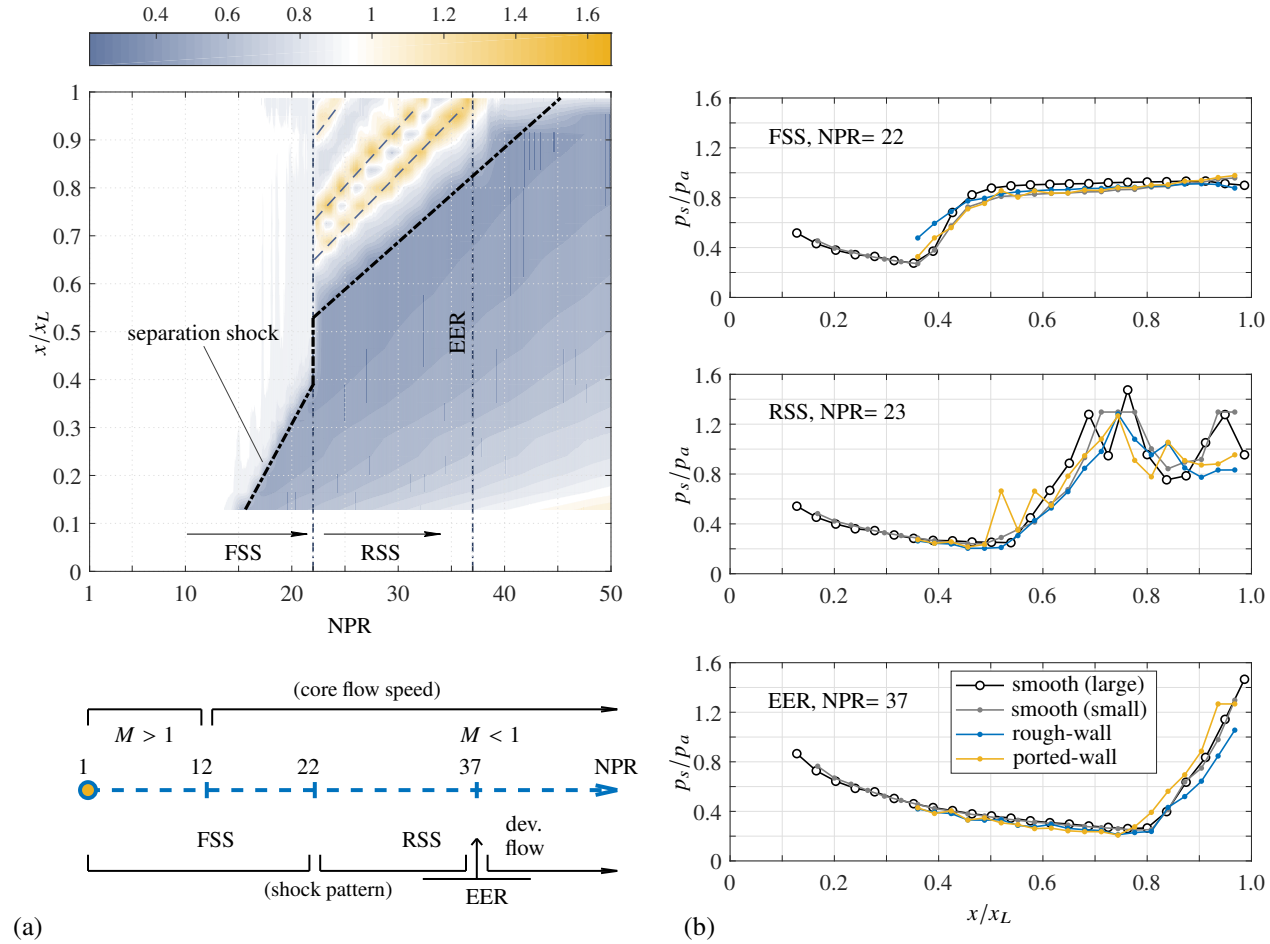

Figure 6: a) Static wall pressure (p_s/p_a) during startup of the large, smooth-wall TOP nozzle. b) Comparison of static wall pressures (p_s/p_a) corresponding to FSS, RSS and EER flow states of all TOP nozzles.

which occurs every time a trapped annular separation bubble is pushed out of the nozzle. Eventually the last separation bubble approaches the nozzle lip and establishes the onset of the end-effects-regime. This generates the most significant off-axis side-loads during nozzle startup since this last separation bubble is the largest of all bubbles (due to the shape of the expansion and compression waves that bound it) and therefore allows the largest pressure gradient to form. For this TOP nozzle contour, the onset of EER occurs at NPR 37 as seen in Fig. 6a. Static wall pressure profiles at discrete instances during nozzle startup are also shown in Fig. 6b. In this case, the wall pressure corresponding to the different nozzles are shown overlaid one another. Close inspection reveals discrepancies on account of surface roughness effects, though the agreement is qualitatively good considering the scale of these nozzles.

3.2 Dynamic wall pressure

The dynamic wall pressure near the nozzle exit was captured using a Kulite model XT-140 dynamic pressure transducer installed 0.2 inches from the nozzle lip, as shown in Fig. 1. This model Kulite has a 100 psia (±0.1% FS) dynamic

range and was sampled simultaneously at a rate of $f_s = 20$ kHz using a National Instruments PXI system. The protective B-type screen on this transducer, with 2.62 mm outside diameter, was flush with the interior surfaces of the nozzles. Sample pressure time histories of the normalized instantaneous pressure ($\tilde{p}/p_a$) are shown in Fig. 7 for the three nozzles the kulite sensors (see Table 1). As these are absolute pressure readings, each startup and shutdown of the nozzle measures fluctuations superposed a transient (time-dependent) mean flow, and at a time scale that is easily separable from the dynamic components. Thus, an eighth-order Chebyshev Type 1 lowpass filter is used to separate the static pressure reading into its mean P and fluctuating components p', where $\tilde{p} = P + p'$. The filtering process is shown in Fig. 7a and is the same one used by Tinney (2017).[27]

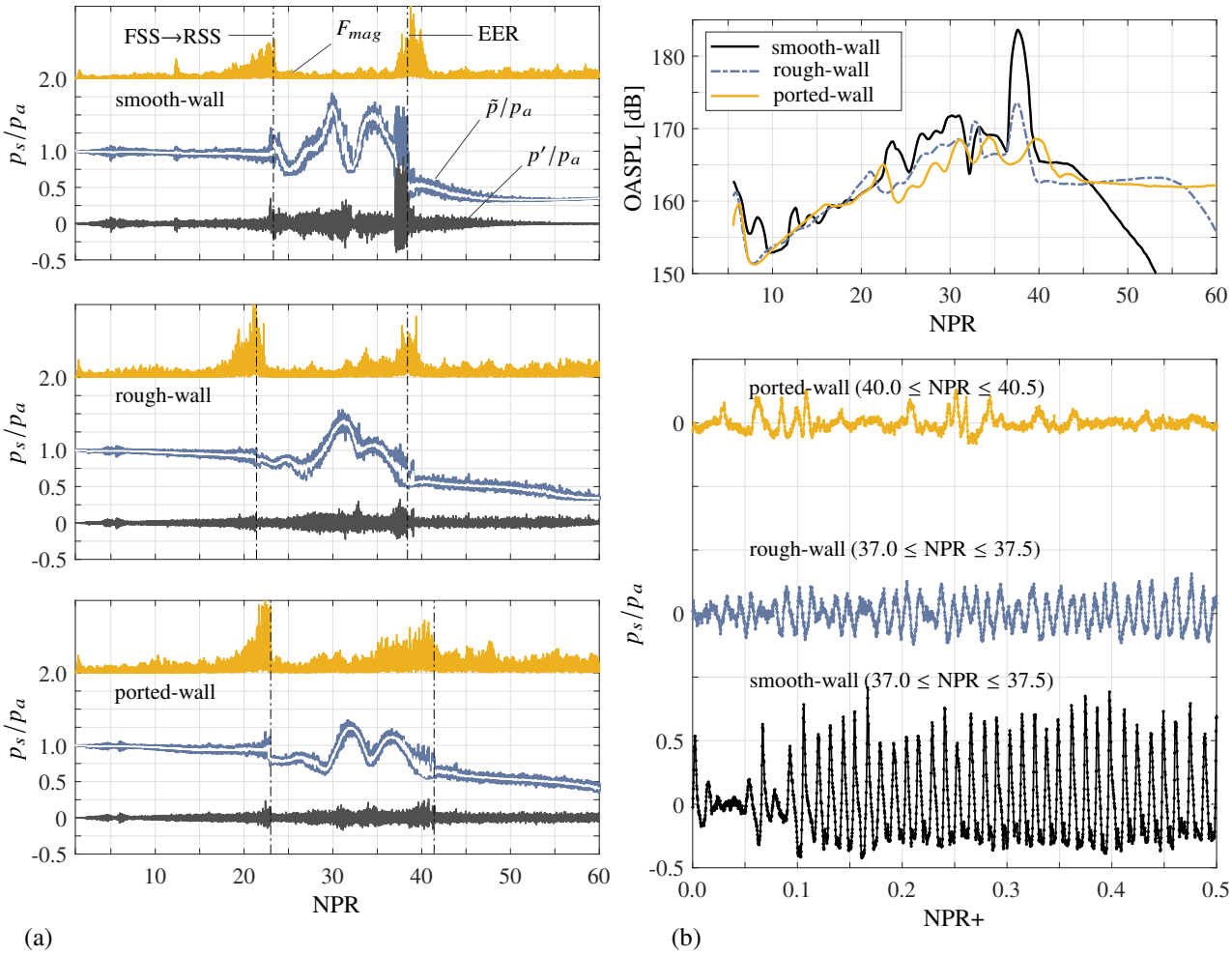

Figure 7: (a) Kulite pressure reading during startup and overall sound pressure level [dB] of all tests for the small-TOP nozzle, (b) Pressure time series during end-effects for all small nozzles.

For the smooth-wall nozzle in Fig. 7a, the first abrupt change in the instantaneous wall pressure occurs after FSS→RSS transition, as identified by the first dashed line in each illustration. Remaining transients reflect changes to the wall pressure as different features of the RSS shock structure pass over this region of the nozzle. From the standpoint of the unsteady wall pressure, the end-effects regime is identified by the occasion when the wall shock pulsates in and out of the nozzle. For the smooth-wall nozzle in Fig. 7a, this generates a distinct tone between 37.0 ≤ NPR ≤ 39; identical findings were reported by Rojo et al. (2016)[23] for the same nozzle. The OASPL (average of all twenty runs per nozzle and discretized by 0.1 NPR) is shown in Fig. 7b-top and reveals a peak of 183.6 dB with this nozzle during EER. Closer inspection of the pressure signal in Fig. 7a is shown in Fig. 7b-bottom, where it is confined to the EER event and is shown to exhibit highly harmonic behavior corresponding to axial displacements of the separation shock along the nozzle wall. From peak to valley, the pressure range is approximately 1.3 atmospheres of pressure. For the rough-wall nozzle, the pulsations lose amplitude (peak OASPL of 173.5 dB and a peak to valley pressure range of 0.50 atmospheres) this suggesting that, for this scale nozzle, surface roughness effects may be impacting the measurements. A high speed digital camera recorded the nozzles during testing and showed no visible motions of the nozzles thus

suggesting that these reductions are not the consequence of changes to the nozzle geometry or wall deflections.

Moving on to the ported-wall nozzle, additional reductions in unsteady pressure are observed with a peak average OASPL of 168.6 dB. In this case, EER is delayed to higher nozzle pressure ratios with the onset of EER related loads appearing to occur around NPR 40. EER pulsations are less periodic and appear intermittently with a peak to valley pressure range of 0.32 atmospheres. Thus, surface roughness effects are shown to reduce vibroacoustic loads with additional reductions being invoked by the insertion of pressure relief ports in the vicinity of the EER shock.

Nozzle side-load magnitudes $F_m = (F_x^2 + F_y^2)^{0.5}$ are also reported in Fig. 7a (normalized by their respective maximum values). For now, side-load amplitudes are not important, as opposed to the alignment of high side-load events with the unsteady pressure near the nozzle lip. For the smooth-wall nozzle, FSS→RSS transition is identified by a sharp drop in nozzle side-loads, which aligns in time with abrupt changes to the mean wall pressure due to the attachment of the RSS flow structure to the nozzle wall where the kulite sensor resides. Thus, wall pressure unsteadiness at the nozzle lip manifests a response that is in phase with nozzle side-loads and is void of surface roughness effects, or the insertion of pressure relief ports at the nozzle lip. On the contrary, nozzle side-loads generated by the smooth-wall nozzle during EER continue to persist well after separation shock pulsations vanish. The same artifact is observed in the rough-wall nozzle. Albeit, the insertion of pressure relief ports near the nozzle exit is shown to cause both unsteady wall pressures and nozzle side-loads to occur at roughly the same instant in time. A plausible explanation is that the intermittent-like motions of the wall shock, due to the insertion of pressure relief ports during EER, are interfering destructively with nozzle side-load resonance.

3.3 Time-frequency analysis

A time-frequency analysis of the unsteady lip wall pressure is now evaluated using wavelet transforms to see what tones are affected by wall roughness effects and the pressure relief ports. The process is thoroughly described elsewhere (see Farge 1992[28] and Addison 2002[29]) and has been used extensively by Baars et al. (2013,2015)[19,21] to study shock-wave boundary layer interactions in high area-ratio nozzles, like the ones studied here. For the wavelet analysis here, the time-dependent fluctuating wall pressure $p'(t)$ is convolved with a mother wavelet $\psi(t/l)$ to produce wavelet coefficients,

$$\tilde{p}\,(l,t) = \int p\,(t')\,\psi^*\left(\frac{t'-t}{l}\right)dt \tag{14}$$

where l in Eq. (14) is the time-scale of the wavelet. Morlet wavelets, with a central frequency of $\omega_\psi = 6$, are used and are formed by modulating a sinusoidal plane wave by way of a Gaussian,

$$\psi(t/l) = e^{j\omega_\psi t/l}e^{-|t/l|^2/2} \tag{15}$$

Like many other popular wavelet shapes, the Morlet wavelet has an analytical solution in the fourier domain which replaces the convolution with the products of fourier coefficients to reduce processor time. Here the convolution is performed using 121 scales distributed logarithmically over the frequency range 10 Hz $< f < f_s/2$, where $f_s = 20$ kHz. The resultant Wavelet Power Spectrum (WPS) is computed as follows,

$$E\,(l,t) = \frac{|\tilde{p}\,(l,t)\,|^2}{l} \tag{16}$$

from which the double-sided WPS is determined by $E\,(f,t)$. The findings are plotted in Fig. 8 where each wavelet spectrogram represents the average wavelet power spectra from all twenty startups of one of the nozzles. Only regions inside the cone of influence are shown and are constructed by overlapping signal partitions comprising N^{14} samples. For transients encompassing small time-scales, the time-averaged double sided wavelet spectra is calculated using $\overline{E} = \frac{1}{T}\int_T E dt$, where T is the window in time over which the averaging is performed and is referred to as a Global Wavelet Power Spectra(GWPS).

Starting with the WPS in Fig. 8, three windows are identified in each of the spectrograms and correspond to FSS flow between 20 ≤ NPR ≤ 22 (window 1), the EER event (unique to each nozzle) and post EER flow between 45 ≤ NPR ≤ 47 (window 3) when the separation shock is anchored to the nozzle lip and is beginning to flow full. Both FSS (window 1) and post-EER (window 3) flows are shown to generate relatively broadband wall pressure spectra for all three nozzles and is reflective of a stationary turbulent boundary layer. On the other hand, the EER event, as captured by window 2 for the smooth-wall nozzle in Fig. 8a, reveals a 370 Hz tone with a maximum amplitude of 156.8 dB at NPR 37.6. A second peak at 740 Hz is a higher harmonic of the fundamental 370 Hz tone, and with an amplitude of 148 dB. It is unclear what the source of the higher harmonic is, though it may have something to do with a small skip in the fore or aft motion of the separation shock cycle during EER. Where the rough-wall nozzle in Fig. 8b is concerned,

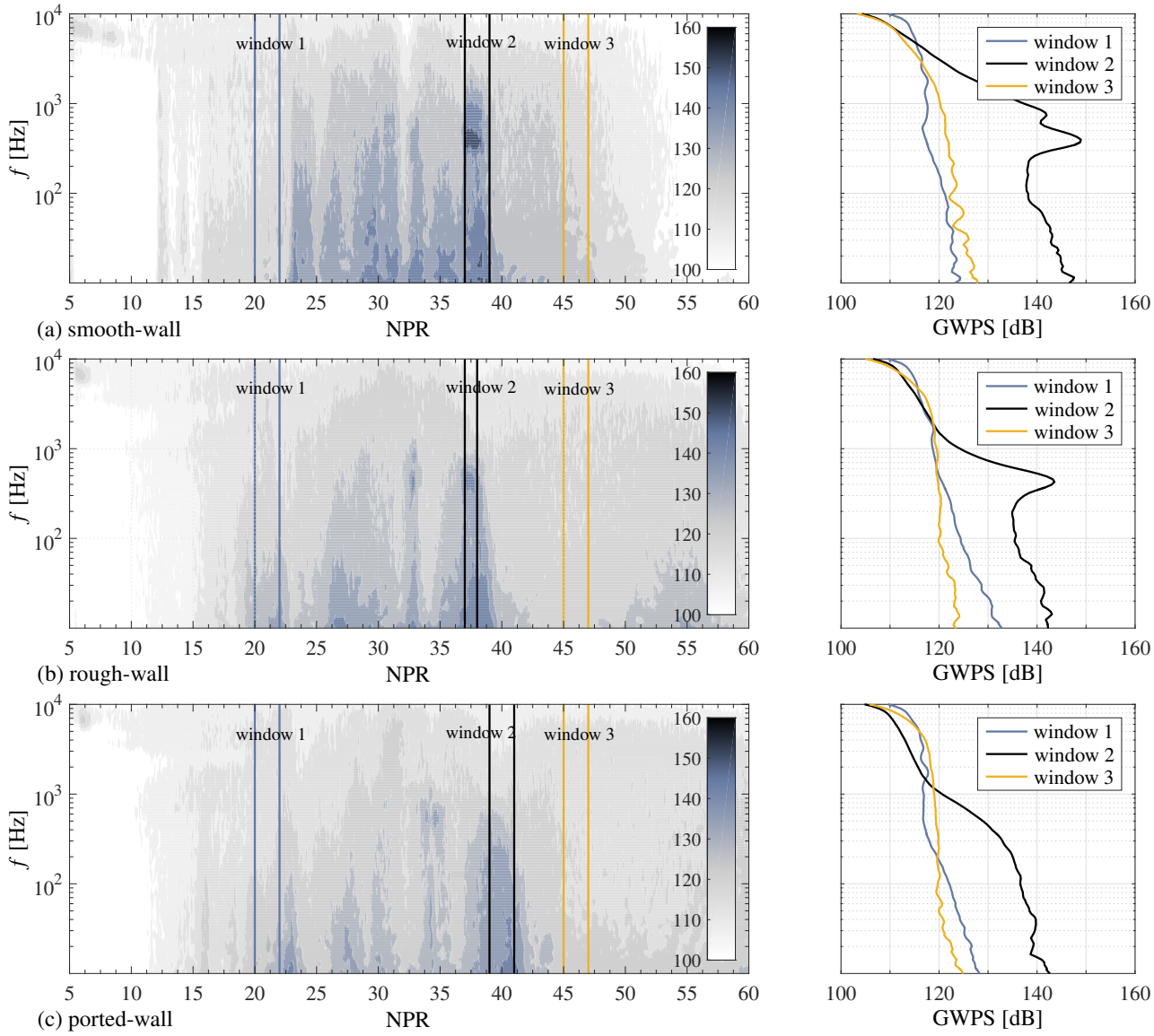

Figure 8: Wavelet power spectra [dB] of the unsteady lip pressure during startup of the (a) smooth-wall, (b) rough-wall, and (c) ported-wall nozzles. Global Wavelet Power Spectra [dB], averaged over the three windows identified in the WPS.

a similar EER tone is observed in window 2 at NPR 37.4, but at a frequency of 425 Hz with a peak amplitude of 146.6 dB. Thus, the effect of surface roughness is a 10 dB reduction in the EER tone with an upward shift in the fundamental frequency and a removal of the higher harmonic. As for the ported-wall nozzle in Fig. 8c, GWPS from window 2 is void of EER tones and is generated by averaging the WPS between $39 \leq \text{NPR} \leq 41$.

3.4 Nozzle side-loads

Nozzle startup side-loads are now shown in Fig. 9 for all nozzle types. For each of the twenty startups, side load magnitudes are computed and then segmented into bin widths of $\delta\text{NPR} = 0.50$. Thus, a total of twenty measurement points are available for each NPR bin between $10 \leq \delta\text{NPR} \leq 60$. In Fig. 9, dark lines identify the limits of the data spread while peak values during both FSS→RSS transition and EER are tabulated in Table 2. Starting with Fig. 9a, the smooth-wall nozzle is shown to generate significant side loads during both FSS→RSS transition and EER, with side load magnitudes during EER being approximately 1.76 times greater than the ones generated during FSS→RSS transition. Tare nozzle side loads are also shown and are consistently within 2 [lbf] over all nozzle pressure ratios; tare nozzle side loads are comparable to the side loads generated during RSS and post-EER flow of the smooth-wall nozzle. This reinforces the fact, in the absence of skewed shock induced side loads, nozzle side loads are generated

by boundary layer turbulence. In Fig. 9b side loads generated by the rough-wall nozzle demonstrate that the peak side-load during FSS→RSS transition is a factor of 1.88 times the peak EER load. This is the opposite observation to the smooth-wall nozzle whose maximum peak side-loads occurred during EER; aside from this being a surface roughness effect, the exact mechanisms responsible for this discrepancy is unknown. Nevertheless, both the smooth-wall and rough-wall nozzles generate peak EER side loads at NPR 38.75, while the rough-wall nozzle generates an additional side load of 4.7 lbf at NPR 33.5. This additional side-load at lower NPR corresponds to intermittent venting of the first trapped annular separation bubble with the ambient and was observed during side-load testing of large-scale smooth-wall nozzles (not shown). This suggests that boundary layer Reynolds number effects may limit the usability of the small smooth-wall nozzle. There is some indication that similar discrepancies were observed by Stark and Genin (2016)[30] in the separation length of a truncated ideal contour nozzle when evaluated at two different scales.

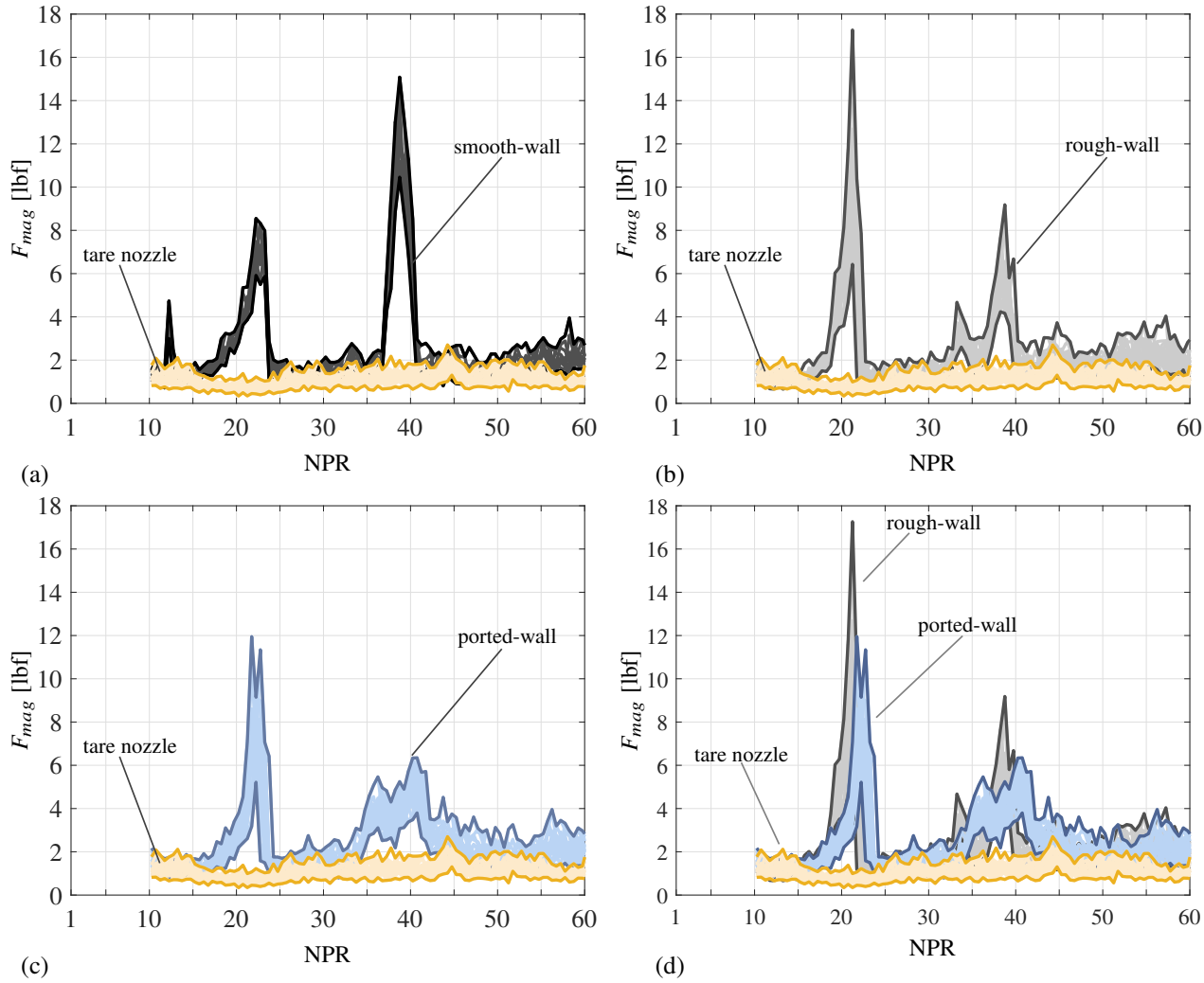

Figure 9: Maximum and minimum force magnitude (F_{mag}) side-loads recorded by the (a) smooth-wall, (b) rough-wall, and (c) ported-wall nozzles during startup. (d) Comparison between rough-wall and ported-wall nozzles.

In Fig. 9c, side loads generated by the ported-wall nozzle are shown, and then again in Fig. 9d where they are compared to the rough-wall nozzle. The comparison in Fig. 9d may provide the best indicator of the performance of the pressure relief ports at reducing nozzle side-loads because of concerns over boundary layer Reynolds number effects. For FSS→RSS transition in Fig. 9d, a 35% reduction in peak nozzle side-loads is achieved with the ported-wall nozzle during startup and at a pressure ratio that is 0.5 NPR higher than the rough-wall nozzle. As for EER peak side-loads, the ported-wall nozzle provides a 31% reduction relative to the rough-wall nozzle with another shift to higher pressure ratios by 1.5 NPR. It is postulated that the ported-wall nozzle serves as a pathway for transferring flow mass from within the separation bubble to the low pressure regions located upstream of the wall shock to reduce fore and aft motions of the EER separation shock. As NPR increase, so too does the pressure differential between the port openings when port openings straddle the separation shock. Flow measurements or high fidelity simulations would help to explain the mechanism responsible for reducing these side loads, but are currently unavailable.

No.	nozzle	(FSS→RSS) NPR	F_{mag} [lbf]	(EER) NPR	F_{mag} [lbf]
2	smooth-wall	22.25	8.55	38.75	15.10
3	rough-wall	21.25	17.26	38.75	9.18
4	ported-wall	21.75	11.95	40.25	6.34
5	tare	20.75	1.34	38.25	1.98

Table 2: **Summary of maximum side-loads measured by different nozzle hardware during startup.**

4. Conclusions

A first principals understanding of the effect of wall pressure relief ports on nozzle side loads is evaluated for a thrust optimized parabolic contour nozzle. These ports are inserted near the nozzle lip where the separation shock resides during EER flow and are intended to passively vent gases from the high pressure separation bubble to the low pressure region upstream of the shock. The venting of gas lowers the pressure differential thereby reducing the fore and aft motions of the separation shock responsible for generating off-axis side loads. A 5 dB reduction in the unsteady wall pressure at the nozzle lip is observed with the use of the pressure relief ports, relative to the baseline, rough-wall nozzle, thereby demonstrating how they have the potential of reducing vibroacoustic loads on nearby structures. The reductions are attributed to visible shifts from strong tone-like pressure waveforms (observed with both the smooth-wall and rough-wall nozzles) to waveforms that are more intermittent and broadband with the use of pressure relief ports. For the smooth-wall nozzle, a delayed response in the onset of EER pulsations, relative to the time when the nozzle responds structurally to these pulsations, is observed. This reinforces the notion that additional reductions in nozzle side loads may be accomplished by reducing the exposure time of the nozzle to EER loads.[31] However, the delay disappears in the case of the rough-wall and ported-wall nozzles thus suggesting that differences in the EER pulsation frequency relative to the nozzle natural frequency may be an important factor to consider. Between the rough-wall and ported-wall nozzles, a 35% reduction in peak side loads is recorded during FSS→RSS transition while a 31% reduction recorded during EER is achieved with the ported-nozzle. A parametric study that explores changes to nozzle side loads on account of the number of ports, their location(s) in the nozzle wall, port orifice size, shape, and orientation, is warranted if further improvements to this prototype device are to be made.

References

[1] Frey, M., and Hagemann, G. (2000) "Restricted shock separation in rocket nozzles," *Journal Propulsion & Power,* Vol. 16, No. 3, pp. 478-484.

[2] Verma, S.B., and Haidn, O. (2009) "Study of Restricted Shock Separation Phenomena in a Thrust Optimized Parabolic Nozzle," *Journal Propulsion & Power,* Vol. 25, No. 5, pp. 1046-1057.

[3] Martelli, E., Nasuti, F., and Onofri, M. (2010) "Numerical Calculation of FSS/RSS Transition in Highly Overexpanded Rocket Nozzle Flows," *Journal of Shock Waves,* Vol. 20, No. 2, pp. 139-146. doi:10.1007/s00193-009-0244-4

[4] Baars, W.J., Tinney, C.E., Ruf, J.H., Brown, A.M., and McDaniels, D.M. (2012) "Wall pressure unsteadiness and side loads in overexpanded rocket nozzles," *AIAA Journal,* Vol. 50, No. 1, pp. 61-73.

[5] Ruf, J.H., McDaniels, D.M., and Brown, A.M. (2010) "Details of Side Load Test Data and Analysis for a Truncated Ideal Contour Nozzle and a Parabolic Contour Nozzle," *AIAA Paper 2010-6813*.

[6] Blades, E.L., Luke, E.A., and Ruf, J. (2012) "Fully Coupled Fluid-Structure Interaction Simulation of Rocket Engine Side Loads," *AIAA Paper 2012-3969*.

[7] Tinney, C.E., Scott, K., Routon, M., Sirohi, J., and Ruf, J. (2017) "Effect of Aeroelasticity on Vibroacoustic Loads during Startup of Large Area Ratio Nozzles," *AIAA Paper 2017-3361*.

[8] Eitner, M., Miller, B., Sirohi, J., Tinney, C.E. (2021) "Effect of broad-band phase-based motion magnification on modal parameter estimation," *MSSP Journal,* Vol. 146, No. 106995, pp. 1-14.

[9] Foster, C.R., and Cowles, F.B. (1949) "Experimental study of gas-flow separation in overexpanded exhaust nozzles for rocket motors," *NASA PR-N4-103*.

[10] Horn, M., Fisher, S. (1993) “Dual-bell altitude compensating nozzles," *NASA TR-N94-23057*.

[11] Cimini, M., Martelli, E., and Bernardini, M., (2021) “Numerical Analysis of Side-Load Reductions in a Subscale Dual-bell Rocket Nozzle," *Flow, Turbulence and Combustion,* Vol. 107, pp. 551-574, doi:10.1007/s10494-021-00243-4

[12] Legros, B., Léger, L., Kourta, A., Sefir, A., Sellam, M., and Chpoun, A. (2022) “Fluidic control of flow regime transition and retransition in a dual-bell launcher nozzle," *8th Space Propulsion Conference*, HAL Id: hal-04040496.

[13] Ivanov, I.E., and Kryukov, I.A. (2019) “Numerical study of ways to prevent side loads in an over-expanded rocket nozzles during the launch stage," *Acta Astronautica,* Vol. 163, pp. 196-201, doi:10.1016/j.actaastro.2019.02.032

[14] Hadjadj, A., Perrot, Y., and Verma, S. (2015) “Numerical study of shock/boundary layer interaction in supersonic overexpanded nozzles," *Aerospace Science and Technology,* Vol. 42, pp. 158-168, doi:10.1016/j.ast.2015.01.010

[15] Stark, R., and Génin, C. (2011) “Experimental Study on Rocket Nozzle Side Load Reduction ," *AIAA Paper 2011-0389*.

[16] Stark, R., and Génin, C. (2016) “Optimization of a Rocket Nozzle Side Load Reduction Device," *AIAA Journal*. Vol. 32, No. 6, pp. 1395-1402, doi:10.2514/1.B35971

[17] Valdez, J., and Tinney, C.E. (2018) “Measurements of a Mach 3 jet using high-speed optical flow techniques," *AIAA Paper 2018-3148*.

[18] Baars, W.J., and Tinney, C.E. (2014) “Shock-structures in the acoustic field of a Mach 3 jet with crackle," *J. Sound & Vib.*, Vol. 333, pp. 2539-2552.

[19] Baars, W.J., and Tinney, C.E. (2013) “Transient wall pressure in an overexpanded and large area-ratio nozzle," *Exp. Fluids,* Vol. 54, No. 1468, pp. 1-17.

[20] Donald, B.W., Baars, W.J., Tinney, C.E., and Ruf, J.H. (2014) “Sound produced by large area-ratio nozzles during fixed and transient operations," *AIAA Journal,* Vol. 52, No. 7, pp. 1474-1485.

[21] Baars, W.J., Ruf, J.H., and Tinney, C.E. (2015) “Non-stationary shock motion unsteadiness in an axisymmetric geometry with pressure gradient," *Exp. Fluids,* Vol. 56, No. 92, pp. 1-18.

[22] Canchero, A., Tinney, C.E., Murray, N., and Ruf, J.H. (2016) “Flow and acoustics of clustered rockets during startup," *AIAA Journal,* Vol. 54, No. 5, pp. 1660-1669.

[23] Rojo, R., Tinney, C.E., and Ruf, J.H. (2016) “Effect of Stagger on the Vibroacoustic Loads from Clustered Rockets," *AIAA Journal,* Vol. 54, No. 11, pp. 3588-3597.

[24] Ruf, J.H., McDaniels, D.M. and Brown, A.M. (2009) “Nozzle side load testing and analysis at Marshall Space Flight Center," *AIAA Paper 2009-4856*.

[25] Dumnov, G.E. (1996) “Unsteady Side-Loads Acting on the Nozzle with Developed Separation Zone," *AIAA Paper 1996-3220*.

[26] Ruf, J.H., McDaniels, D.M. and Brown, A.M. (2010) “Cold Flow Test Results for Nozzle Side Loads for J-2X and SSME Test Articles," *57th JANNAF PropulsionMeeting/5th Liquid Propulsion Subcommittee*, May.

[27] Tinney, C.E. (2017) “Wall Pressure Unsteadiness on the Aft Deck of a Planar Multi-stream Supersonic Nozzle," *AIAA Paper 2017-0525*.

[28] Farge, M. (1992) “Wavelet Transforms and Their Application to Turbulence," *Annual Review of Fluid Mechanics,* Vol. 24, pp. 395-458. doi:10.1146/annurev.fl.24.010192.002143

[29] Addison, P. S. (2002) “The Illustrated Wavelet Transform Handbook," Taylor and Francis, New York, pp. 1-353.

[30] Stark, R.H., and Génin, C., (2016) “Scaling Effects on Side Load Generation in Subscale Rocket Nozzles," *AIAA Paper 2016-4669*, doi:10.2514/6.2016-4669

[31] Wang, T.-S., (2009) “Transient three-dimensional startup side load analysis of a regeneratively cooled nozzle," *Shock Waves,* Vol. 19, pp. 251-264, doi:10.1007/s00193-009-0201-2

[32] Canchero, A., Tinney, C.E., Murray, N., and Ruf, J.H. (2016) “Acoustic Imaging of Clustered Rocket Nozzles Undergoing End Effects," *AIAA Journal,* Vol. 54, No. 12,pp. 3778-3786.